

# Epipolar Geometry from Profiles under Circular Motion

Paulo R. S. Mendonça\*, Kwan-Yee K. Wong and Roberto Cipolla

Department of Engineering, University of Cambridge

Cambridge, UK, CB2 1PZ

[prdsm2, kykw2, cipolla]@eng.cam.ac.uk

February 13, 2001

## Abstract

This paper addresses the problem of motion estimation from profiles (also known as apparent contours) of an object rotating on a turntable in front of a single camera. Its main contribution is the development of a practical and accurate technique for solving this problem from profiles alone, which is precise enough to allow the reconstruction of the shape of the object. No correspondences between points or lines are necessary, although the method proposed can be used equally when these features are available, without any further adaptation. Symmetry properties of the surface of revolution swept out by the rotating object are exploited to obtain the image of the rotation axis and the homography relating epipolar lines in 2 views, in a robust and elegant way. These, together with geometric constraints for images of rotating objects, are then used to obtain first

---

\*Corresponding author

the image of the horizon, which is the projection of the plane that contains the camera centers, and then the epipoles, thus fully determining the epipolar geometry of the image sequence. The estimation of the epipolar geometry by this sequential approach (image of rotation axis — homography — image of the horizon — epipoles) avoids many of the problems usually found in other algorithms for motion recovery from profiles. In particular, the search for the epipoles, by far the most critical step, is carried out as a simple one-dimensional optimization problem. The initialization of the parameters is trivial and completely automatic for all stages of the algorithm. After the estimation of the epipolar geometry, the Euclidean motion is recovered using the fixed intrinsic parameters of the camera, obtained either from a calibration grid or from self-calibration techniques. Finally, the spinning object is reconstructed from its profiles, using the motion estimated in the previous stage. Results from real data are presented, demonstrating the efficiency and usefulness of the proposed methods.

**Keywords:** structure and motion, epipolar geometry, profiles, apparent contours, circular motion.

## 1 Introduction

Methods for motion estimation and 3D reconstruction from point or line correspondences in a sequence of images have achieved a high level of sophistication, with impressive results [35, 21, 14]. Nevertheless, if corresponding points are not available the current techniques cannot be applied. That is exactly the case when the scene being viewed is composed by non-textured smooth surfaces, and in this situation the dominant feature in the image is the *profile* or *apparent contour* of the surface [22]. Besides, even when point correspondences can be established, the profile still offers

important clues for determining both motion and shape, and therefore it should be used whenever available.

The first attempts to estimate motion from profiles date back to Rieger, in 1986 [30], who introduced the concept of a *frontier point*, interpreted as “centers of spin” [*sic*] of the image motion. The paper dealt with the case of fronto-parallel orthographic projection. This idea was further developed by Porrill and Pollard [29], who recognized the frontier point as a fixed point on the surface, corresponding to the intersection of two consecutive *contour generators* [7]. The connection between the epipolar geometry and the frontier points was established in [17], and an algorithm for motion estimation from profiles under perspective projection was introduced in [6]. Related works also include [2], where a technique based on registering the images using a planar curve was first developed. This method was implemented in [11], which also showed results of reconstruction from the estimated motion. The work in [19] presents a method where the affine approximation is used to bootstrap the full projective case.

This work presents a method for estimating the motion of an object rotating around a fixed axis from information provided by its profiles alone. It makes use of symmetry properties [41, 12, 15] of the surface of revolution swept out by the rotating object to overcome the main difficulties and drawbacks present in other methods which have attempted to estimate motion from profiles, namely: (1) the need for a very good initialization for the epipolar geometry and an unrealistic demand for a large number of *epipolar tangencies* [6, 2, 1] (here as few as two epipolar tangencies are needed); (2) restriction to linear motion [31] (whereas circular motion is a more practical situation); or (3) the use of an affine approximation [39] (which may be used only for shallow scenes).

An interesting comparison can be made between the work presented here and [14]. Both papers tackle the same problem, but while in [14] hundreds of points were tracked

and matched for each pair of adjacent images, it will be shown here that a solution can be obtained even when only two epipolar tangencies are available, with at least comparable results.

## 1.1 Outline of the Paper

This paper begins by describing a method to obtain the image of the rotation axis and the coordinates of a special vanishing point, used in the parameterization of the fundamental matrix under circular motion, from symmetry properties of the profile of the surface of revolution swept out by an object placed on a turntable. These provide the homography component of the fundamental matrix in a *plane plus parallax* [9, 36] representation. The epipolar constraint is then used to estimate the epipoles for each pair of images in the sequence. These epipoles should be collinear, and the line containing them corresponds to the horizon. Due to noise, this alignment will not be verified, and a line is robustly fitted to the cloud of epipoles to provide an estimate for the horizon. Once this estimate is available, the epipolar constraint is again employed to recompute the epipoles with a minimal parameterization specialized to circular motion [38]. The epipoles are now constrained to lie on the horizon, providing an accurate estimate for the epipolar geometry of each pair of images in the sequence. Intrinsic parameters, either computed from a self-calibration algorithm or precomputed by any standard calibration technique, can then be used together with the fundamental matrices to determine the camera motion.

Section 2 reviews the symmetry properties exhibited by the image of a surface of revolution. Section 3 establishes the relationship between this transformation and the epipolar geometry, and also presents two useful parameterizations of the fundamental matrix. These parameterizations allow the estimation of the epipoles to be carried out as independent one-dimensional searches, avoiding local minima and greatly reducing

the computational complexity of the estimation. Section 4 presents the algorithm for motion recovery, and the implementation of the algorithm for real data is shown in Section 5, which also makes comparisons with previous works. Experimental results using the estimated motion for reconstruction are shown in Section 6.

## 2 Symmetry in the Image of a Surface of Revolution

An object rotating about a fixed axis sweeps out a surface of revolution [15]. Symmetry properties of the image of this surface of revolution can be exploited to estimate the parameters of the motion of the object in a simple and elegant way, as will be shown next. In the definitions that follow, points and lines will be referred to by their representation as vectors in homogeneous coordinates.

A 2D homography that keeps the pencil of lines through a point  $\mathbf{v}$  and the set of points on a line  $\mathbf{l}$  fixed is called a *perspective collineation* with center  $\mathbf{v}$  and axis  $\mathbf{l}$ . A *homology* is a perspective collineation whose center and axis are not incident (otherwise the perspective collineation is called an *elation*). Let  $\mathbf{a}$  be a point mapped by a homology onto a point  $\mathbf{a}'$ . It is easy to show that the center of the homology,  $\mathbf{u}$ , and the points  $\mathbf{a}$  and  $\mathbf{a}'$  are collinear. Let  $\mathbf{q}_a$  be the line passing through these points, and  $\mathbf{v}_a$  be the intersection of  $\mathbf{q}_a$  and the axis  $\mathbf{l}$ . If  $\mathbf{a}$  and  $\mathbf{a}'$  are harmonic conjugates with respect to  $\mathbf{v}$  and  $\mathbf{v}_a$ , i.e., their cross-ratio is one, the homology is said to be a *harmonic homology* (see details in [32, 10] and also Fig. 1(a)). The matrix  $\mathbf{W}$  representing a harmonic homology with center  $\mathbf{v}$  and axis  $\mathbf{l}$  in homogeneous coordinates is given by

$$\mathbf{W} = \mathbf{I} - 2 \frac{\mathbf{v}\mathbf{l}^T}{\mathbf{v}^T\mathbf{l}}. \quad (1)$$

Henceforth a matrix representing a projective transformation in homogeneous coordi-

nates will be used in reference to the transformation itself whenever an ambiguity does not arise.

The profile of a surface of revolution exhibits a special symmetry property, which can be described by a harmonic homology [24]. The next theorem gives a formal definition for this property:

**Theorem 1** *The profile of a surface of revolution  $S$  viewed by a pinhole camera is invariant to the harmonic homology with axis given by the image of the rotation axis of the surface of revolution and center given by the image of the point at infinity in a direction orthogonal to a plane that contains the rotation axis and the camera center.*

The following lemma will be used in the proof of Theorem 1.

**Lemma 1** *Let  $\mathbf{T} : \Gamma' \mapsto \Gamma'$  be a harmonic homology with axis  $\mathbf{l}'$  and center  $\mathbf{v}'$  on the plane  $\Gamma'$ , and let  $\mathbf{H} : \Gamma' \mapsto \Gamma$  be a bijective 2D homography between the planes  $\Gamma'$  and  $\Gamma$ . Then, the transformation  $\mathbf{W} = \mathbf{H}\mathbf{T}\mathbf{H}^{-1} : \Gamma \mapsto \Gamma$  is a harmonic homology with axis  $\mathbf{l} = \mathbf{H}^{-\mathbf{T}}\mathbf{l}'$  and center  $\mathbf{v} = \mathbf{H}\mathbf{v}'$ .*

**Proof:** Since  $\mathbf{H}$  is bijective,  $\mathbf{H}^{-1}$  exists. Then

$$\begin{aligned} \mathbf{W} &= \mathbf{H} \left( \mathbb{I} - 2 \frac{\mathbf{v}'\mathbf{l}'^{\mathbf{T}}}{\mathbf{v}'^{\mathbf{T}}\mathbf{l}'} \right) \mathbf{H}^{-1} \\ &= \mathbb{I} - 2 \frac{\mathbf{v}\mathbf{l}^{\mathbf{T}}}{\mathbf{v}^{\mathbf{T}}\mathbf{l}}, \end{aligned} \quad (2)$$

since  $\mathbf{v}^{\mathbf{T}}\mathbf{l} = \mathbf{v}'^{\mathbf{T}}\mathbf{l}'$ . □

The following corollary is a trivial consequence of Lemma 1:

**Corollary 1** *Let  $\mathbf{T}$ ,  $\mathbf{H}$ ,  $\mathbf{W}$ ,  $\Gamma'$  and  $\Gamma$  be defined as in Lemma 1. The transformation  $\mathbf{H}$  is an isomorphism between the structures  $(\mathbf{T}, \Gamma')$  and  $(\mathbf{W}, \Gamma)$ , i.e.,  $\forall \gamma \in \Gamma'$ ,  $\mathbf{H}\mathbf{T}\gamma = \mathbf{W}\mathbf{H}\gamma$ .*

An important consequence of Lemma 1 and Corollary 1 is that if a set of points  $\hat{s}$ , e.g., the profile of a surface of revolution, is invariant to a harmonic homology  $\mathbf{T}$ , the set  $s$  obtained by transforming  $\hat{s}$  by a 2D projective transformation  $\mathbf{H}$  is invariant to the harmonic homology  $\mathbf{W} = \mathbf{H}\mathbf{T}\mathbf{H}^{-1}$ .

Without loss of generality assume that the axis of rotation of the surface of revolution  $S$  is coincident with the  $y$ -axis of a right-handed orthogonal coordinate system. Considering a particular case of Theorem 1 in which the pinhole camera  $\hat{\mathbf{P}}$  [13] is given by  $\hat{\mathbf{P}} = [\mathbb{I} | \mathbf{t}]$ , where  $\mathbf{t} = [0 \ 0 \ \alpha]^T$ , for any  $\alpha > 0$ , symmetry considerations show that the profile  $\hat{s}$  of  $S$  will be bilaterally symmetric with respect to the image of the  $y$ -axis [28, 26], which corresponds to the line  $\mathbf{q}_s = [1 \ 0 \ 0]^T$  in (homogeneous) image coordinates.

**Proof of Theorem 1 (particular case):** Since  $\hat{s}$  is bilaterally symmetric about  $\mathbf{q}_s$ , there is a transformation  $\mathbf{T}$  that maps each point of  $\hat{s}$  onto its symmetric counterpart, given by

$$\mathbf{T} = \begin{bmatrix} -1 & 0 & 0 \\ 0 & 1 & 0 \\ 0 & 0 & 1 \end{bmatrix}. \quad (3)$$

However, as any bilateral symmetry transformation,  $\mathbf{T}$  is also a harmonic homology, with axis  $\mathbf{q}_s$  and center  $\mathbf{u}_x = [1 \ 0 \ 0]^T$ , since

$$\mathbf{T} = \mathbb{I} - 2 \frac{\mathbf{u}_x \mathbf{q}_s^T}{\mathbf{u}_x^T \mathbf{q}_s}. \quad (4)$$

The transformation  $\mathbf{T}$  maps the set  $\hat{s}$  onto itself (although the points of  $\hat{s}$  are not mapped onto themselves by  $\mathbf{T}$ , but onto their symmetric counterparts), and thus  $\hat{s}$  is invariant to the harmonic homology  $\mathbf{T}$ . Since the camera center lies on the  $z$ -axis

of the coordinate system, the plane that contains the camera center and the axis of rotation is in fact the  $yz$ -plane, and the point at infinity orthogonal to this plane is  $\mathbf{U}_x = [1 \ 0 \ 0 \ 0]^T$ , whose image is  $\mathbf{u}_x$ .  $\square$

Let  $\mathbf{P}$  be an arbitrary pinhole camera. The camera  $\mathbf{P}$  can be obtained by rotating  $\hat{\mathbf{P}}$  about its optical center by a rotation  $\mathbf{R}$  and transforming the image coordinate system of  $\hat{\mathbf{P}}$  by introducing the intrinsic parameters represented by the calibration matrix  $\mathbf{K}$  [13]. Let  $\mathbf{KR} = \mathbf{H}$ . Thus,  $\mathbf{P} = \mathbf{H}[\mathbf{I} \ | \ \mathbf{t}]$ , and the point  $\mathbf{U}_x$  in space with image  $\mathbf{u}_x$  in  $\hat{\mathbf{P}}$  will project to a point  $\mathbf{v}_x = \mathbf{H}\mathbf{u}_x$  in  $\mathbf{P}$ . Analogously, the line  $\mathbf{q}_s$  in  $\hat{\mathbf{P}}$  will correspond to a line  $\mathbf{l}_s = \mathbf{H}^{-T}\mathbf{q}_s$  in  $\mathbf{P}$ . It is now possible to derive the proof of Theorem 1 in the general case.

**Proof of Theorem 1 (general case):** Let  $s$  be the profile of the surface of revolution  $S$  obtained from the camera  $\mathbf{P}$ . Thus, the counter-domain of the bijection  $\mathbf{H}$  acting on the profile  $\hat{s}$  is  $s$  (or  $\mathbf{H}\hat{s} = s$ ), and, using Lemma 1, the transformation  $\mathbf{W} = \mathbf{HTH}^{-1}$  is a harmonic homology with center  $\mathbf{v}_x = \mathbf{H}\mathbf{u}_x$  and axis  $\mathbf{l}_s = \mathbf{H}^{-T}\mathbf{q}_s$ . Moreover, from Corollary 1,  $\mathbf{WH}\hat{s} = \mathbf{HT}\hat{s}$ , or  $\mathbf{W}s = \mathbf{HT}\hat{s}$ . From the particular case of the Theorem 1 it is known that the profile  $\hat{s}$  will be invariant to the harmonic homology  $\mathbf{T}$ , so  $\mathbf{W}s = \mathbf{H}\hat{s} = s$ .  $\square$

When the camera is pointing directly towards the axis of rotation, the transformation that maps  $s$  onto its symmetric counterpart will be reduced to a skewed symmetry [20, 27, 5], which corresponds to a particular case of the harmonic homology in which the pole is at infinity. It is given by

$$\mathbf{S} = \frac{1}{\cos(\phi - \rho)} \begin{bmatrix} -\cos(\phi + \rho) & -\sin(\phi + \rho) + \sin(\phi - \rho) & 2d \cos \phi \\ -\sin(\phi + \rho) - \sin(\phi - \rho) & \cos(\phi + \rho) & 2d \sin \phi \\ 0 & 0 & \cos(\phi - \rho) \end{bmatrix} \quad (5)$$



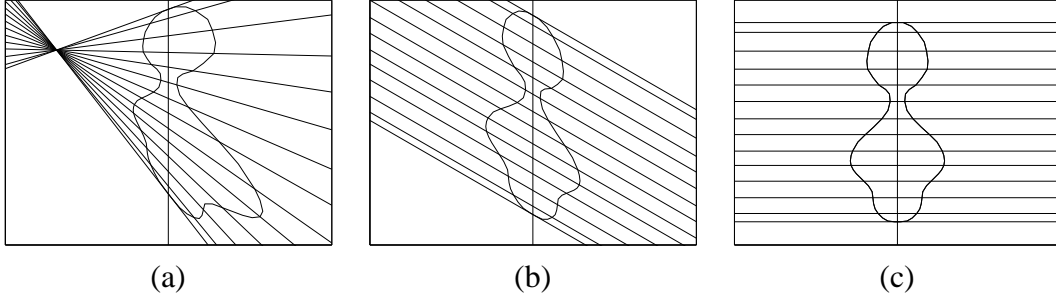


Figure 1: (a) Profile of a surface of revolution under general viewing conditions. The symmetry of the profile is represented by a harmonic homology defined by the image of the rotation axis and the pole. (b) When the camera is pointing towards the axis of rotation the transformation reduces to a skewed symmetry, which is a particular case of the harmonic homology with the pole at infinity. (c) If, additionally, the camera has zero skew and aspect ratio one, the transformation becomes a bilateral symmetry, in which the lines of symmetry are perpendicular to the image of the rotation axis.

where  $\mathbf{l}_s = [\cos \rho \quad \sin \rho \quad -d]^T$  is the image of the rotation axis, with  $d = u_0 \cos \rho + v_0 \sin \rho$ . The angle  $\phi$  gives the orientation of the *lines of symmetry*, which are the lines joining each point to its skew-symmetric counterpart (see Fig. 1(b)). The transformation  $\mathbf{S}$  has 3 degrees of freedom (dof).

If the camera also has zero skew and aspect ratio 1, the transformation is further reduced to a bilateral symmetry, given by

$$\mathbf{B} = \begin{bmatrix} -\cos 2\rho & -\sin 2\rho & 2d \cos \rho \\ -\sin 2\rho & \cos 2\rho & 2d \sin \rho \\ 0 & 0 & 1 \end{bmatrix}. \quad (6)$$

The transformation now has only 2 dof, since the lines of symmetry are orthogonal to  $\mathbf{l}_s$ . A graphical representation of the bilateral symmetry, skewed symmetry and harmonic homology is shown in Fig. 1.

### 3 Parameterizations of the Fundamental Matrix

#### 3.1 Fundamental Matrix under Circular Motion

The fundamental matrix corresponding to a pair of cameras related by a rotation around a fixed axis has a very special parameterization, as shown in [38, 14], which can be expressed explicitly in terms of fixed image features under circular motion (image of rotation axis, pole and horizon, jointly holding 5 dof) and the relative angle of rotation (1 dof). A simpler derivation of this result will be shown here. Moreover, a novel parameterization based on the harmonic homology will be introduced, providing a connection between the geometry of the complete sequence (harmonic homology) with the geometry of a single pair of images (fundamental matrix).

Consider the pair of camera matrices  $\hat{\mathbf{P}}_1$  and  $\hat{\mathbf{P}}_2$ , given by

$$\begin{aligned}\hat{\mathbf{P}}_1 &= [\mathbb{I} | \mathbf{t}] \\ \hat{\mathbf{P}}_2 &= [\mathbf{R}_y(\theta) | \mathbf{t}],\end{aligned}\tag{7}$$

where

$$\begin{aligned}\mathbf{t} &= \begin{bmatrix} 0 & 0 & 1 \end{bmatrix}^T \text{ and} \\ \mathbf{R}_y(\theta) &= \begin{bmatrix} \cos \theta & 0 & \sin \theta \\ 0 & 1 & 0 \\ -\sin \theta & 0 & \cos \theta \end{bmatrix},\end{aligned}\tag{8}$$

for  $\theta \neq 0$ . Let  $\hat{\mathbf{F}}$  be the fundamental matrix relating  $\hat{\mathbf{P}}_1$  and  $\hat{\mathbf{P}}_2$ . From (7) and (8), it is

easy to see that

$$\hat{\mathbf{F}} = \begin{bmatrix} 0 & \cos \theta - 1 & 0 \\ \cos \theta - 1 & 0 & \sin \theta \\ 0 & -\sin \theta & 0 \end{bmatrix} \quad (9)$$

$$= -\sin \theta \begin{bmatrix} 1 \\ 0 \\ 0 \end{bmatrix}_{\times} + (\cos \theta - 1) \left( \begin{bmatrix} 1 \\ 0 \\ 0 \end{bmatrix} [0 \ 1 \ 0] + \begin{bmatrix} 0 \\ 1 \\ 0 \end{bmatrix} [1 \ 0 \ 0] \right) \quad (10)$$

Let  $\mathbf{U}_x$ ,  $\mathbf{U}_y$  and  $\mathbf{U}_z$  be the points at infinity in the  $x$ ,  $y$  and  $z$  direction, respectively, in world coordinates. Projecting these points using the camera  $\hat{\mathbf{P}}_1$ , we obtain the vanishing points  $\mathbf{u}_x$ ,  $\mathbf{u}_y$  and  $\mathbf{u}_z$  given by

$$\mathbf{u}_x = \begin{bmatrix} 1 \\ 0 \\ 0 \end{bmatrix}, \mathbf{u}_y = \begin{bmatrix} 0 \\ 1 \\ 0 \end{bmatrix} \text{ and } \mathbf{u}_z = \begin{bmatrix} 0 \\ 0 \\ 1 \end{bmatrix}. \quad (11)$$

The image of the horizon is the line  $\mathbf{q}_h$ , and the image of the rotation axis is the line  $\mathbf{q}_s$ , where

$$\mathbf{q}_s = \begin{bmatrix} 1 \\ 0 \\ 0 \end{bmatrix} \text{ and } \mathbf{q}_h = \begin{bmatrix} 0 \\ 1 \\ 0 \end{bmatrix}. \quad (12)$$

Substituting (11) and (12) into (10), the desired parameterization is obtained:

$$\hat{\mathbf{F}} = -\sin \theta \left[ [\mathbf{u}_x]_{\times} + \tan \frac{\theta}{2} (\mathbf{q}_s \mathbf{q}_h^T + \mathbf{q}_h \mathbf{q}_s^T) \right]. \quad (13)$$

The factor “ $-\sin \theta$ ” can be eliminated since the fundamental matrix is defined only up to an arbitrary scale. Assume now that the cameras  $\hat{\mathbf{P}}_1$  and  $\hat{\mathbf{P}}_2$  are transformed by a rotation  $\mathbf{R}$  about their optical centers and the introduction of a set of intrinsic parameters represented by the calibration matrix  $\mathbf{K}$ . The new pair of cameras,  $\mathbf{P}_1$  and  $\mathbf{P}_2$ , is related to  $\hat{\mathbf{P}}_1$  and  $\hat{\mathbf{P}}_2$  by

$$\begin{aligned}\mathbf{P}_1 &= \mathbf{H}\hat{\mathbf{P}}_1 \text{ and} \\ \mathbf{P}_2 &= \mathbf{H}\hat{\mathbf{P}}_2,\end{aligned}\tag{14}$$

where  $\mathbf{H} = \mathbf{KR}$ . The fundamental matrix  $\mathbf{F}$  of the new pair of cameras  $\mathbf{P}_1$  and  $\mathbf{P}_2$  is given by

$$\begin{aligned}\mathbf{F} &= \mathbf{H}^{-\text{T}}\hat{\mathbf{F}}\mathbf{H}^{-1} \\ &= \det(\mathbf{H})[\mathbf{v}_x]_{\times} + \tan \frac{\theta}{2}(\mathbf{l}_s\mathbf{l}_h^{\text{T}} + \mathbf{l}_h\mathbf{l}_s^{\text{T}}),\end{aligned}\tag{15}$$

where  $\mathbf{v}_x = \mathbf{H}\mathbf{u}_x$ ,  $\mathbf{l}_h = \mathbf{H}^{-\text{T}}\mathbf{q}_h$  and  $\mathbf{l}_s = \mathbf{H}^{-\text{T}}\mathbf{q}_s$ . Since the fundamental matrix is defined only up to a scale factor, (15) can be rewritten as

$$\mathbf{F}(\theta) = [\mathbf{v}_x]_{\times} + \kappa \tan \frac{\theta}{2}(\mathbf{l}_s\mathbf{l}_h^{\text{T}} + \mathbf{l}_h\mathbf{l}_s^{\text{T}}),\tag{16}$$

where  $\kappa = 1/\det(\mathbf{H})$ . The notation  $\mathbf{F}(\theta)$  was used in (16) to emphasize that, for a given circular motion sequence, the parameters  $\mathbf{v}_x$ ,  $\mathbf{l}_s$ ,  $\mathbf{l}_h$  and  $\kappa$  are fixed, and the fundamental matrices associated with any pair of cameras in the sequence differs only in the value of  $\theta$ .

### 3.2 Parameterization via Planar Harmonic Homology

The images of a rotating object are the same as the images of a fixed object taken by a camera rotating around the same axis, or by multiple cameras along that circular trajectory. Consider any two of such cameras, denoted by  $\mathbf{P}_1$  and  $\mathbf{P}_2$ . If  $\mathbf{P}_1$  and  $\mathbf{P}_2$  point towards the axis of rotation and have zero skew and aspect ratio 1, their epipoles  $\mathbf{e}_1$  and  $\mathbf{e}_2$  will be symmetric with respect to the image of the rotation axis, or  $\mathbf{e}_2 = \mathbf{T}\mathbf{e}_1$ , according to Fig. 2. In a general situation, the epipoles will simply be related by the transformation  $\mathbf{e}_2 = \mathbf{W}\mathbf{e}_1$ . It is then straightforward to show that the corresponding epipolar lines  $\mathbf{l}_1$  and  $\mathbf{l}_2$  are related by  $\mathbf{l}_2 = \mathbf{W}^{-T}\mathbf{l}_1$ . This means that the pair of epipoles can be represented with only two parameters once  $\mathbf{W}$  is known. From (1) it can be seen that  $\mathbf{W}$  has only four dof.

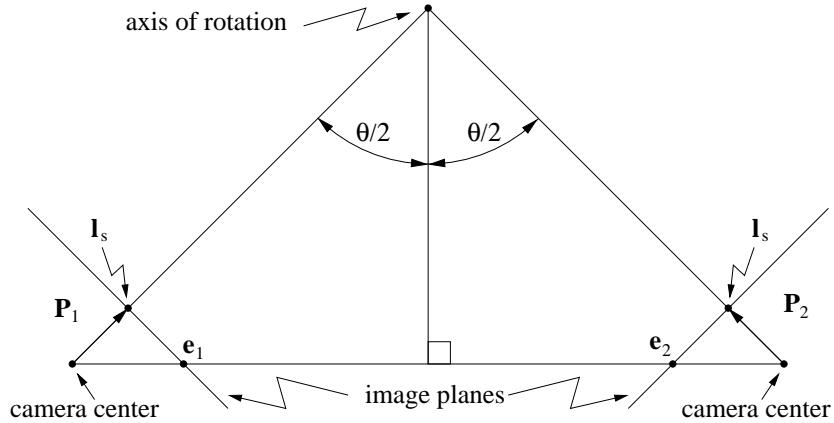


Figure 2: If the cameras are pointing towards the axis of rotation and their skew is zero and aspect ratio is 1, the epipoles  $\mathbf{e}_1$  and  $\mathbf{e}_2$  are symmetric with respect to the image of the rotation axis.

In [25, 40] it has been shown that any fundamental matrix  $\tilde{\mathbf{F}}$  can be parameterized as  $\tilde{\mathbf{F}} = [\tilde{\mathbf{e}}']_{\times} \tilde{\mathbf{M}}$  in a plane plus parallax parameterization, where  $\tilde{\mathbf{M}}^{-T}$  is any matrix that maps the epipolar lines from one image to the other, and  $\tilde{\mathbf{e}}'$  is the epipole in the

second image. It follows that

$$\mathbf{F} = [\mathbf{e}_2]_{\times} \mathbf{W}, \quad (17)$$

where, from (16),  $\mathbf{e}_2 = \mathbf{v}_x - \kappa \tan \frac{\theta}{2} [\mathbf{l}_s]_{\times} \mathbf{l}_h$ . Therefore,  $\mathbf{F}$  has only 6 dof: 4 to determine  $\mathbf{W}$  and 2 to fix  $\mathbf{e}_2$ , in agreement with [38]. Note that in the case of skewed symmetry and bilateral symmetry, the dof of the fundamental matrix will be reduced to 5 and 4 respectively, corresponding to the decrease in the dof of the symmetry transformation. A full account of the dof of the fundamental matrix under different configurations is given in Table 1.

From (17) it can be seen that the transformation  $\mathbf{W}$  corresponds to a plane induced homography (see [18]). This means that the registration of the images can be done by using  $\mathbf{W}$  instead of a planar contour as proposed in [2, 11]. It is known that different choices of the plane that induces the homography in a plane plus parallax parameterization of the fundamental matrix, such as the one in (17), will result in different homographies, although they will all generate the same fundamental matrix, since

$$\mathbf{F} = [\mathbf{e}_2]_{\times} \mathbf{W} = [\mathbf{e}_2]_{\times} [\mathbf{W} + \mathbf{e}_2 \mathbf{b}^T] \quad \forall \mathbf{b} \in \mathbb{R}^3. \quad (18)$$

The 3 parameter family of homographies  $[\mathbf{W} + \mathbf{e}_2 \mathbf{b}^T]$  parameterized in  $\mathbf{b}$  has a one-to-one correspondence with the set of planes in  $\mathbb{R}^3$ . The particular plane that induces the planar homology  $\mathbf{W}$  is given in the next theorem:

**Theorem 2** *The planar homology  $\mathbf{W}$  relating the cameras  $\mathbf{P}_1$  and  $\mathbf{P}_2$  is induced by the plane  $\Xi$  that contains the axis of rotation and bisects the segment joining the optical centers of the cameras.*

**Proof:** The existence and uniqueness of  $\Xi$  satisfying the hypothesis of the Theorem

are trivial. Let  $\mathbf{x}_1 = [1 \ 0 \ 0]^T$ ,  $\mathbf{x}_2 = [0 \ 1 \ 0]^T$ , and  $\mathbf{x}_3 = [0 \ 0 \ 1]^T$ . Without loss of generality, let

$$\begin{aligned}\mathbf{P}_1 &= \mathbf{KR}[\mathbb{I} \mid \mathbf{x}_3] \quad \text{and} \\ \mathbf{P}_2 &= \mathbf{KR}[\mathbf{R}_y^\theta \mid \mathbf{x}_3],\end{aligned}\tag{19}$$

where  $\mathbf{K}$  is the matrix of intrinsic parameters of  $\mathbf{P}_1$  and  $\mathbf{P}_2$ ,  $\mathbf{R}$  is the rotation matrix relating the orientation of the coordinate system of  $\mathbf{P}_1$  to the world coordinate system, and  $\mathbf{R}_y^\theta$  is a rotation by  $\theta$  about the  $y$ -axis of the world coordinate system, i.e.,

$$\mathbf{R}_y^\theta = \begin{bmatrix} \cos \theta & 0 & \sin \theta \\ 0 & 1 & 0 \\ -\sin \theta & 0 & \cos \theta \end{bmatrix}.\tag{20}$$

Therefore,  $\forall \alpha, \beta \in \mathbb{R}$ , the point  $\mathbf{X} = [-\alpha \sin(\theta/2), \beta, \alpha \cos(\theta/2)]^T$  lies on  $\Xi$ . Projecting  $\mathbf{X}$  using  $\mathbf{P}_1$  and  $\mathbf{P}_2$ , one obtains  $\mathbf{u}_1 = \mathbf{KR}(\mathbf{X} + \mathbf{x}_3)$  and  $\mathbf{u}_2 = \mathbf{KR}(\mathbf{R}_y^\theta \mathbf{X} + \mathbf{x}_3)$ .

Since

$$\begin{aligned}\mathbf{R}_y^\theta \mathbf{X} &= \begin{bmatrix} \alpha \sin \theta \cos(\theta/2) - \alpha \cos \theta \sin(\theta/2) \\ \beta \\ \alpha \sin \theta \sin(\theta/2) + \alpha \cos \theta \cos(\theta/2) \end{bmatrix} \\ &= \begin{bmatrix} \alpha \sin(\theta/2) \\ \beta \\ \alpha \cos(\theta/2) \end{bmatrix} = \begin{bmatrix} -1 & 0 & 0 \\ 0 & 1 & 0 \\ 0 & 0 & 1 \end{bmatrix} \mathbf{X},\end{aligned}\tag{21}$$

or  $\mathbf{R}_y^\theta \mathbf{X} = (\mathbb{I} - 2\mathbf{x}_1\mathbf{x}_1^T)\mathbf{X}$ , we have  $\mathbf{u}_2 = \mathbf{KR}[(\mathbb{I} - 2\mathbf{x}_1\mathbf{x}_1^T)\mathbf{X} + \mathbf{x}_3]$ , or  $\mathbf{u}_2 = (\mathbb{I} - 2\mathbf{KR}\mathbf{x}_1\mathbf{x}_1^T\mathbf{R}^{-1}\mathbf{K}^{-1})\mathbf{u}_1$ . It can be shown [26] that  $\mathbf{KR}\mathbf{x}_1 = \mathbf{v}_x$  and  $\mathbf{x}_1^T\mathbf{R}^{-1}\mathbf{K}^{-1} = \mathbf{I}_s^T$ ,

and thus  $\mathbf{u}_2 = \mathbf{W}\mathbf{u}_1$ . □

A graphical representation of the result in Theorem 2 is shown in Fig. 3.

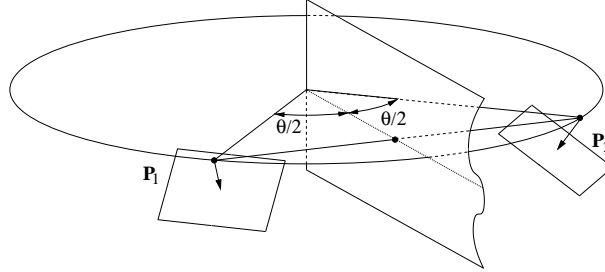


Figure 3: The harmonic homology is a homography induced by the plane that contains the axis of rotation and bisects the segment joining the camera centers.

Configuration	Parameterization	dof
General motion	$[\mathbf{e}]_{\times} \mathbf{M}$	$2 + 5$
Circular motion	$[\mathbf{e}]_{\times} \mathbf{W}$	$2 + 4$
Circular motion with camera pointing at axis of rotation	$[\mathbf{e}]_{\times} \mathbf{S}$	$2 + 3$
Circular motion with camera pointing at axis of rotation and having zero skew and aspect ratio 1	$[\mathbf{e}]_{\times} \mathbf{B}$	$2 + 2$
Circular motion with camera pointing at axis of rotation and having zero skew and no rotation about the optical axis	$[\mathbf{e}]_{\times} \mathbf{B}_0$	$2 + 1$
Pure translation	$[\mathbf{e}]_{\times}$	2
Pure translation orthogonal to optical axis	$[\mathbf{e}_{\infty}]_{\times}$	1

Table 1: Analysis of the dof of the fundamental matrix for different types of motion with fixed intrinsic parameters.

### 3.3 Epipolar Geometry and Profiles of Surfaces

So far the discussion of epipolar geometry and parameterizations of the fundamental matrix under circular motion is applicable to arbitrary image features, such as points



or profiles, as it does not consider particular aspects of the issue when the only image features available are profiles. This section briefly reviews some of the main geometric components of epipolar geometry from profiles.

Consider a surface  $\mathcal{S}$  of type  $C^1$  viewed by two pinhole cameras  $\mathbf{P}_1$  and  $\mathbf{P}_2$ . The following definitions apply [8]:

- a *contour generator* associated with the surface  $\mathcal{S}$  and the camera  $\mathbf{P}_1$  corresponds to the space curve  $\mathcal{C} \subset \mathcal{S}$  such that for all points  $\mathbf{C} \in \mathcal{C}$  the line passing through the optical center of  $\mathbf{P}_1$  and  $\mathbf{C}$  is tangent to  $\mathcal{S}$  at  $\mathbf{C}$ ;
- the image of the contour generator associated with the camera  $\mathbf{P}_1$  is a *profile* or *apparent contour*;
- if two contour generators associated with the surface  $\mathcal{S}$  and the cameras  $\mathbf{P}_1$  and  $\mathbf{P}_2$  intersect, the points of intersection are denoted *frontier points*;
- the epipolar plane  $\Pi$  defined by the optical centers of the two cameras  $\mathbf{P}_1$  and  $\mathbf{P}_2$  and an associated frontier point  $\mathbf{X}_f$  is tangent to the surface  $\mathcal{S}$  at  $\mathbf{X}_f$ ;
- the epipolar lines corresponding to the epipolar plane  $\Pi$  are tangent to their associated profiles and are called *epipolar tangents*;

The tangency points of corresponding epipolar tangents are the images of the same point on the surface  $\mathcal{S}$ , namely the frontier point. The above definitions are illustrated in Fig. 4.

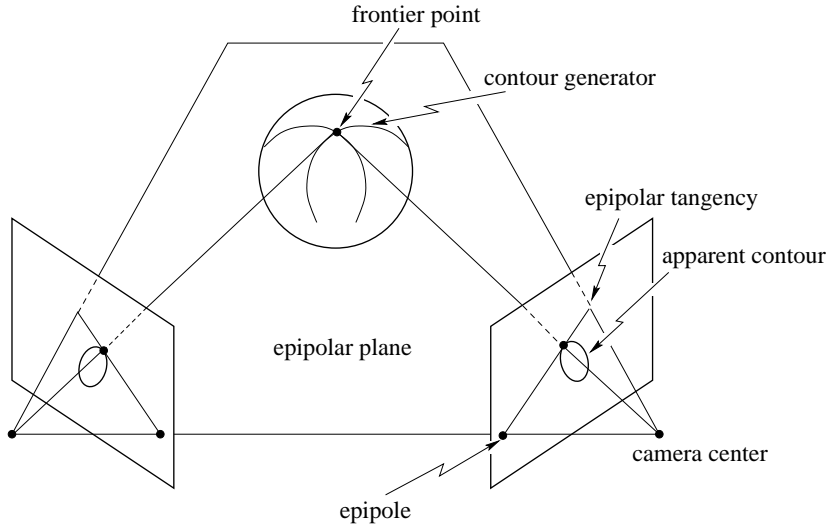


Figure 4: The frontier point is a fixed point on the surface, corresponding to the intersection of two contour generators. The epipolar plane at the frontier point is tangent to the surface, and therefore corresponding epipolar lines are tangent to the profiles.

## 4 Motion Estimation

### 4.1 Estimation of the Harmonic Homology

Consider an object that undergoes a full rotation around a fixed axis. The envelope  $\epsilon$  of its profiles is found by overlapping the images of the sequence and applying a Canny edge detector [4] to the resultant image. This envelope corresponds to the image of a surface of revolution, and thus it is harmonically symmetric. The homography  $\mathbf{W}$  related to  $\epsilon$  is then found by sampling  $N$  points  $\mathbf{x}_i$  along  $\epsilon$  and optimizing the cost function

$$f_{\mathbf{W}}(\mathbf{v}_x, \mathbf{l}_s) = \sum_{i=1}^N \text{dist}(\epsilon, \mathbf{W}(\mathbf{v}_x, \mathbf{l}_s)\mathbf{x}_i)^2, \quad (22)$$

where  $\text{dist}(\epsilon, \mathbf{W}(\mathbf{v}_x, \mathbf{l}_s)\mathbf{x}_i)$  is the orthogonal distance between the curve  $\epsilon$  and the transformed sample point  $\mathbf{W}(\mathbf{v}_x, \mathbf{l}_s)\mathbf{x}_i$ . The estimation of  $\mathbf{W}$  is summarized in Al-

gorithm 1.

The initialization of the line  $\mathbf{l}_s$  and the point  $\mathbf{v}_x$  can be made very close to the global minimum by automatically locating one or more pairs of corresponding bitangents on the envelope. Given two bitangents  $\mathbf{l}(\mathbf{p}_1, \mathbf{p}_2)$  and  $\mathbf{l}(\mathbf{q}_1, \mathbf{q}_2)$  on the two sides of the profile  $\epsilon$  with bitangent points  $\mathbf{p}_1, \mathbf{p}_2$  and  $\mathbf{q}_1, \mathbf{q}_2$ , respectively (see Fig. 5), the intersection of the two bitangents ( $\mathbf{l}(\mathbf{p}_1, \mathbf{p}_2), \mathbf{l}(\mathbf{q}_1, \mathbf{q}_2)$ ) and the intersection of the diagonals ( $\mathbf{l}(\mathbf{p}_1, \mathbf{q}_2), \mathbf{l}(\mathbf{q}_1, \mathbf{p}_2)$ ) give two points defining a line that can be used as an estimate of  $\mathbf{l}_s$ . An estimate for the vanishing point  $\mathbf{v}_x$  is given by the point of intersection of the lines  $\mathbf{l}(\mathbf{p}_1, \mathbf{q}_1)$  and  $\mathbf{l}(\mathbf{p}_2, \mathbf{q}_2)$ . The initialization of  $\mathbf{l}_s$  and  $\mathbf{v}_x$  from bitangents often provides an excellent initial guess for the optimization problem. This is generally good enough to avoid any local minimum and allows convergence to the global minimum in a small number of iterations.

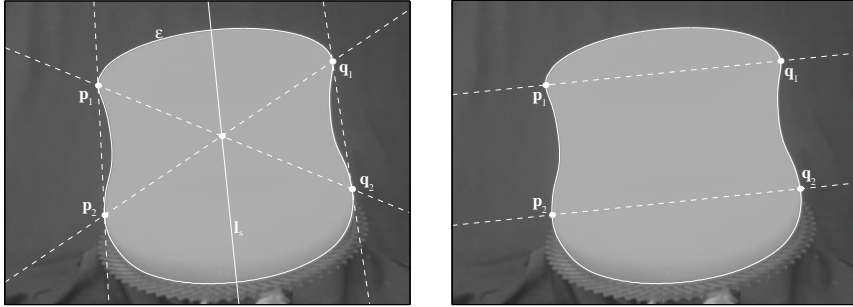


Figure 5: Initialization of the optimization parameters  $\mathbf{l}_s$  and  $\mathbf{v}_x$  from the bitangents and lines formed by bitangent points.

## 4.2 Estimation of the Horizon

After obtaining a good estimation of  $\mathbf{W}$ , one can then search for *epipolar tangencies* between pairs of images in the sequence using the parameterization given by (17). To obtain a pair of corresponding epipolar tangents in two images, it is necessary to find a line tangent to one profile which is transformed by  $\mathbf{W}^{-T}$  to a line tangent to the

---

**Algorithm 1** Estimation of the harmonic homology  $\mathbf{W}$ .
 

---

overlap the images in the sequence;  
 extract the envelope  $\epsilon$  of the profiles using a Canny edge detector;  
 sample  $N$  points  $\mathbf{x}_i$  along  $\epsilon$ ;  
 initialize the axis of symmetry  $\mathbf{l}_s$  and the vanishing point  $\mathbf{v}_x$  using bitangents;  
**while** not converged **do**  
   transform the points  $\mathbf{x}_i$  using  $\mathbf{W}$ ;  
   compute the distances between  $\epsilon$  and the transformed points;  
   update  $\mathbf{l}_s$  and  $\mathbf{v}_x$  to minimize the function in (22);  
**end while**

---

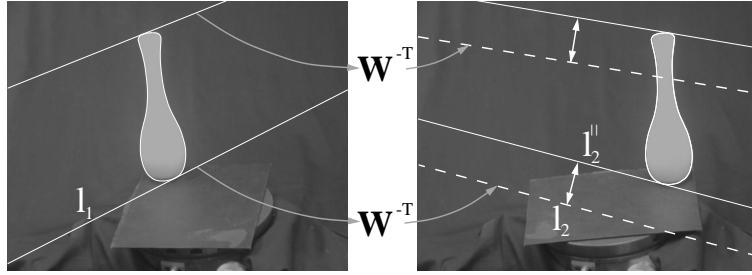


Figure 6: The line  $\mathbf{l}_1$  tangent to the bottom of the profile in the first image is transferred to the line  $\mathbf{l}_2$  in the second image by the harmonic homology. A line  $\mathbf{l}_2^{\parallel}$  parallel to  $\mathbf{l}_2$  and tangent to the bottom of the profile is located and the distance between  $\mathbf{l}_2$  and  $\mathbf{l}_2^{\parallel}$  drives the search for the orientation of  $\mathbf{l}_1$ , which upon convergence will correspond to an epipolar tangent. An epipolar tangent at the top of the profile is obtained in the same way.

profile in the other image (see Fig. 6). The search for corresponding tangents may be carried out as a one-dimensional optimization problem. The single parameter is the angle  $\delta$  that defines the orientation of the epipolar line  $\mathbf{l}_1$  in the first image, and the cost function is given by

$$f_{\mathbf{l}_1}(\delta) = \text{dist}(\mathbf{W}^{-\text{T}}\mathbf{l}_1(\delta), \mathbf{l}_2^{\parallel}(\delta)), \quad (23)$$

where  $\text{dist}(\mathbf{W}^{-\text{T}}\mathbf{l}_1(\delta), \mathbf{l}_2^{\parallel}(\delta))$  is the distance between the transferred line  $\mathbf{l}_2 = \mathbf{W}^{-\text{T}}\mathbf{l}_1$  and a line  $\mathbf{l}_2^{\parallel}$  parallel to  $\mathbf{l}_2$  and tangent to the profile in the second image. Typical values

of  $\delta$  lie between  $-0.5$  rad and  $0.5$  rad, or  $-30^\circ$  and  $30^\circ$ . The shape of the cost function (23) for the profiles in Fig. 6 can be seen in Fig. 7.

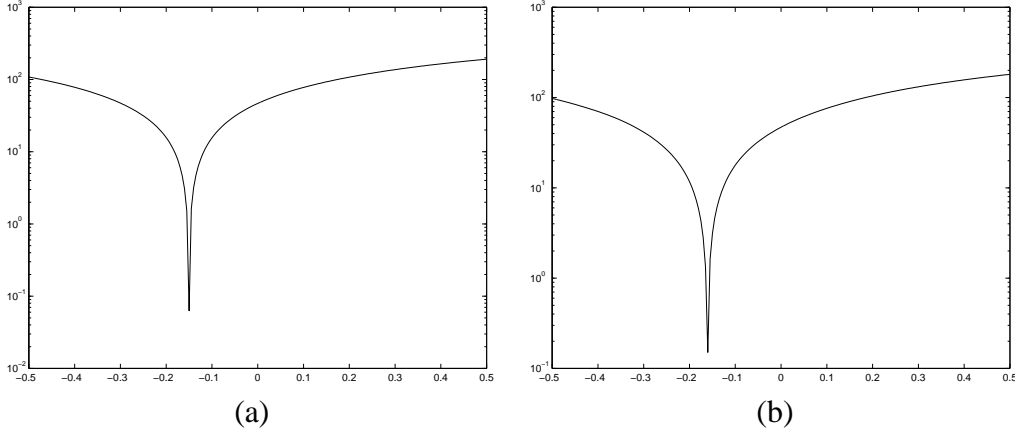


Figure 7: Plot of the cost function (23) for corresponding epipolar tangents near the top (a) and bottom (b) of the profiles in Fig. 6.

---

**Algorithm 2** Estimation of the horizon.

---

```

extract the profiles of the images using a Canny edge detector;
fit B-splines to the top and the bottom of the profiles;
for each selected pair of images do
  initialize  $\delta$ ;
  while not converged do
    find  $\mathbf{l}_1$ ,  $\mathbf{l}_2$  and  $\mathbf{l}_2^\parallel$ ;
    compute the distance between  $\mathbf{l}_2$  and  $\mathbf{l}_2^\parallel$ ;
    update  $\delta$  to minimize the function in (23);
  end while
  compute epipoles;
end for
fit the horizon  $\mathbf{l}_h$  to the cloud of epipoles.

```

---

The epipoles can then be computed as the intersection of epipolar lines in the same image. After obtaining this first estimate for the epipoles, the image of the horizon can then be found by robustly fitting a line  $\mathbf{l}_h$  to the initial set of epipoles, such that  $\mathbf{l}_h^T \mathbf{v}_x = 0$ . Fig. 11 shows a typical output of Algorithm 2, together with the horizon  $\mathbf{l}_h$  fitted to the epipoles.

An alternative method to compute the epipoles is to register the profiles using the homology  $\mathbf{W}$ , eliminating the effects of rotation on the images, and then apply any of the methods in [2, 31, 11], in a plane plus parallax approach. However, no advantage has been obtained by doing so, since to use this method it is necessary to find a common tangent between two profiles, which involves a search at least as complex as the one in Algorithm 2.

### 4.3 Estimation of the Epipoles Constrained to the Horizon

After estimating the horizon, the only missing term in the parameterization of the fundamental matrix shown in (16) is the scale factor

$$\lambda = \kappa \tan \theta / 2. \quad (24)$$

This parameter can be found, again, by a one-dimensional search that minimizes the geometric error of transferred epipolar lines as shown in Fig. 8. Therefore, two distinct parameterizations of the fundamental matrix are used: (17) to obtain the cloud of epipoles and the horizon, and (16) to recompute the position of the epipoles constrained to lie on the horizon.

---

**Algorithm 3** Estimation of the Epipoles.

---

```

for each selected pair of images do
  initialize the scale factor  $\lambda$ ;
  while not converged do
    locate epipolar tangents at the top and the bottom of profiles;
    compute the geometric error as shown in Fig. 8;
    update  $\lambda$  to minimize the geometric error;
  end while
end for

```

---

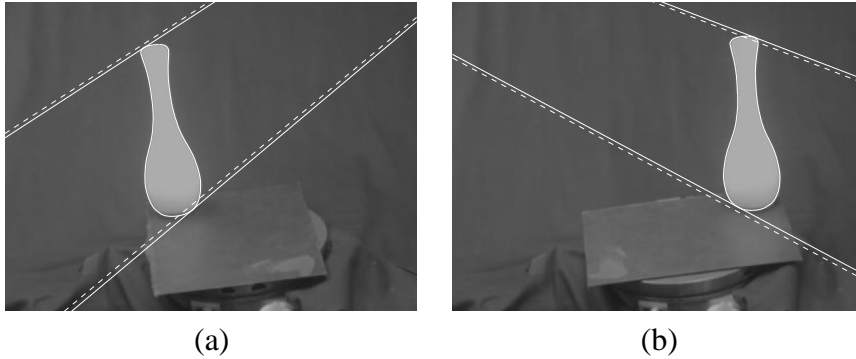


Figure 8: Once the horizon is computed, the location of the epipoles along this line can be refined by using (16). This figure shows the geometric error for transferred epipolar lines. The terms  $\mathbf{v}_x$ ,  $\mathbf{l}_s$  and  $\mathbf{l}_h$  were obtained from Algorithm 1 and Algorithm 2. The solid lines in each correspond to tangents to the profile passing through the putative epipoles, and the dashed lines correspond to lines transferred from one image to the other by applying the harmonic homology  $\mathbf{W}$ . The sum of the distances between transferred lines and the corresponding tangent points is the geometric error that drives the search for the scale factor  $\lambda = \kappa \tan \theta/2$  in (16).

#### 4.4 Limitations of the Algorithm

There are some limitations on the applicability of the algorithms presented here:

**Density of the sequence of images.** If the number of images in the sequence is too small, or the angle of rotation between successive snapshots is too large, the envelope of the profiles no longer approximates the profile of a surface of revolution, and, therefore, Algorithm 1 will fail to correctly estimate the image of the rotation axis and the pole. In practice, this problem does not arise if the angles of rotation in a closed sequence are below  $20^\circ$ . This problem can be overcome by performing a simultaneous search for the harmonic homology and the rotation angles, at the expense of increasing the number of search parameters and therefore the complexity of the optimization.

**Symmetry of the object.** If the object placed on the turntable is rotationally symmetric and its axis of symmetry coincides with the axis of rotation of the turntable,

Algorithm 2 will fail. To understand this problem, consider the alternative formulation of Algorithm 2 in which the epipoles are computed by first registering the images by using the harmonic homology and then computing the epipoles as the intersection of common tangents to the profiles. Under the conditions described above, the registration of the profiles will not produce any effect, since the image of a surface of revolution with the same rotation axis as the turntable is invariant to the harmonic homology. Moreover, the profiles will coincide, and any tangent to one of the profiles will be a common tangent to the pair of profiles. Therefore, the position of the epipole will be undetermined. To avoid this problem it is enough to reposition the symmetric object over the turntable so that its symmetry axis does not coincide anymore with the turntable axis. The further the two axes are, the better. Of course, the placement of the object must not be so distant from the center of the turntable as to remove it from the field of view. In the experiments shown in this paper using a vase and a head model, which are nearly rotationally symmetric in the regions of interest (the top and the bottom of the objects), it was verified that the problem disappears if the axes are separated by a distance of about 50 pixels.

## 5 Implementation and Experimental Results

The algorithms described in the previous section were tested using 2 sets of images from a vase and a head model, respectively (see Fig. 9). Both sets consisted of 36 images, with the turntable rotated by an angle of  $10^\circ$  between successive snapshots. The fact that the angle was fixed was not used either in the estimation of the epipolar geometry, nor in the reconstruction to be shown in Section 6. For the vase sequence, the symmetry transformation associated to the envelope of its profiles was assumed to be a harmonic homology  $\mathbf{W}$ , whereas for the head sequence the transformation was



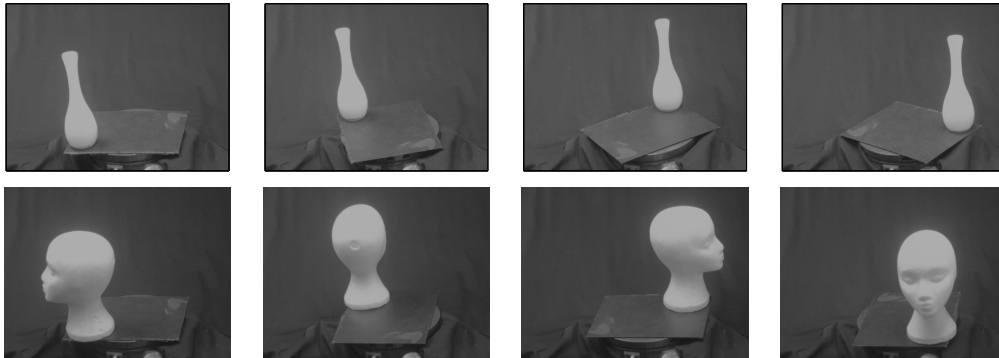


Figure 9: Top row shows 4 images of the vase. Bottom row shows 4 images of the head.

modelled as a skewed symmetry  $\mathbf{S}$ . The choice of the simpler model for the head sequence was motivated by the fact that the camera was nearly pointing towards the axis of the turntable, and therefore the skewed symmetry transformation could be used. Of course, there would have been no problem in adopting the more complex model. To obtain  $\mathbf{W}$  and  $\mathbf{S}$ , Algorithm 1 was implemented with 100 evenly spaced sample points along each envelope ( $N = 100$ ). Initializations were done by using bitangents. Less than 10 iterations of the Levenberg-Marquardt algorithm were necessary, with derivatives computed by finite differences. The final positions of the rotation axes can be seen in Fig. 10.

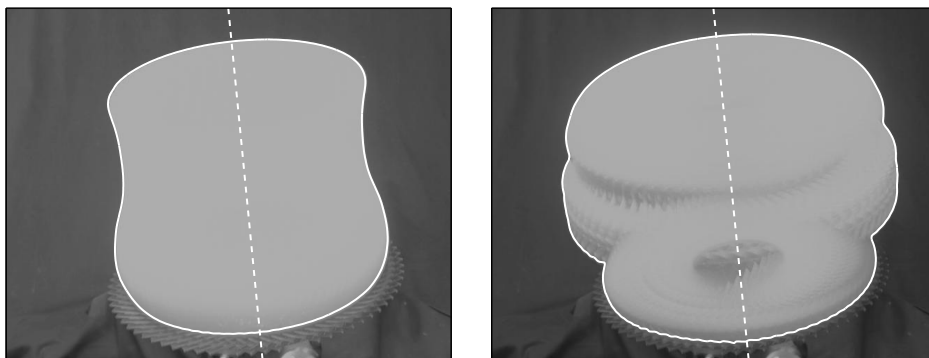


Figure 10: Final configurations for the estimate of the images of the rotation axes for the vase and head sequences.

In the implementation of Algorithm 2, 70 pairs of images were selected by uniformly sampling the indexes of the images in each sequence, and the resultant estimate of the epipoles for the vase sequence is shown in Fig. 11, which also shows the horizon  $\mathbf{l}_h$  found by a robust fit. To get  $\mathbf{l}_h$  a minimization of the median of the squares of the residuals was used, followed by removal of outliers and orthogonal least-squares regression using the remaining points (inliers). The epipolar geometry was then re-estimated with the epipoles constrained to lie on  $\mathbf{l}_h$ . Once the epipolar geometry was obtained, precomputed intrinsic parameters were used to convert the fundamental matrices into essential matrices [13], and these were then decomposed to provide the camera motion and orientation. The resulting camera configurations are presented in Fig. 12.

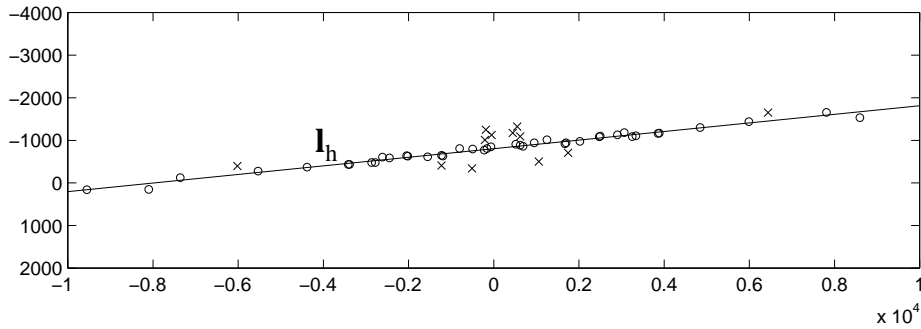


Figure 11: Epipoles estimated by Algorithm 2. The horizon was found by doing a robust fit to the cloud of epipoles. Inliers are shown as circles ( $\circ$ ) and outliers as crosses ( $\times$ ).

The object was rotated on a manual turntable with resolution of  $0.01^\circ$ , but the real precision achieved is highly dependent on the skill of the operator. The RMS errors in the estimated angles were  $0.19^\circ$  and  $0.23^\circ$  for the vase and head sequence respectively (see Fig. 13), demonstrating the accuracy of the estimation.

It is interesting to compare this result with the ones shown in [14, pg. 166] for the “Head”, “Freiburg” and “Dinosaur” sequences, where the average number of point

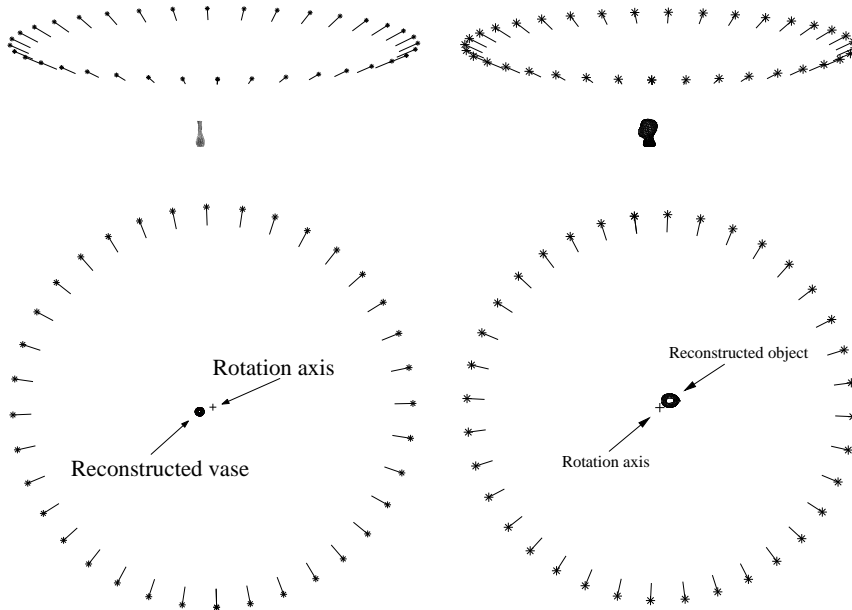


Figure 12: Camera configurations for the vase (left) and head (right) sequences.

matches per image pair varies from 137 to 399, depending on the sequence. It should be stressed that only two epipolar tangents were used for each pair of images in the experiments presented in this paper, with comparable results.

## 6 Reconstruction from Image Profiles

The algorithm for motion estimation introduced here can be used even when point correspondences can be established. On the other hand, methods as the ones in [35], [14] and [21] cannot deal with situations where profiles are the only available features in the scene. Earlier attempts to solve the problem of reconstruction from image profiles under known motion include [16, 37, 7], and state of the art algorithms can be found in [34, 3, 39]. We use a simple method based on triangulation to reconstruct the model using the estimated motion. Examples using voxel-carving [33, 23] are also shown.

Details of the 3D reconstruction of the objects are shown in Fig. 14, Fig. 15 and

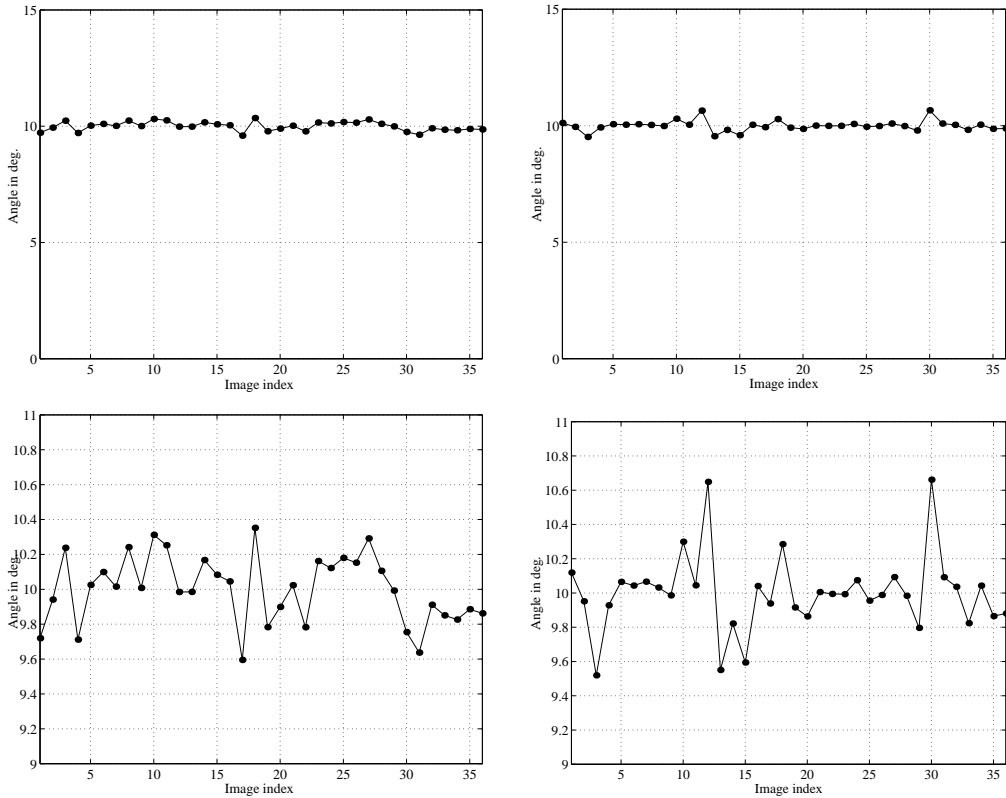


Figure 13: Estimated angles of rotation between successive views for the vase (left) and head (right) sequences, with RMS errors  $0.19^\circ$  and  $0.23^\circ$ , respectively.

Fig. 16. Although no ground truth is available for a quantitative evaluation, it can be seen that the reconstructions are faithful to the images of the objects. As reported in [7], errors in the camera orientation of a few mrad can render the reconstruction useless, therefore confirming the accuracy of the technique introduced here.

## 7 Summary and Conclusions

This paper introduced a novel technique for motion estimation from image profiles. It does not make use of expensive search procedures, such as bundle adjustment, although it naturally integrates data from multiple images. The method is mathematically sound, practical and highly accurate. From the motion estimation to the model

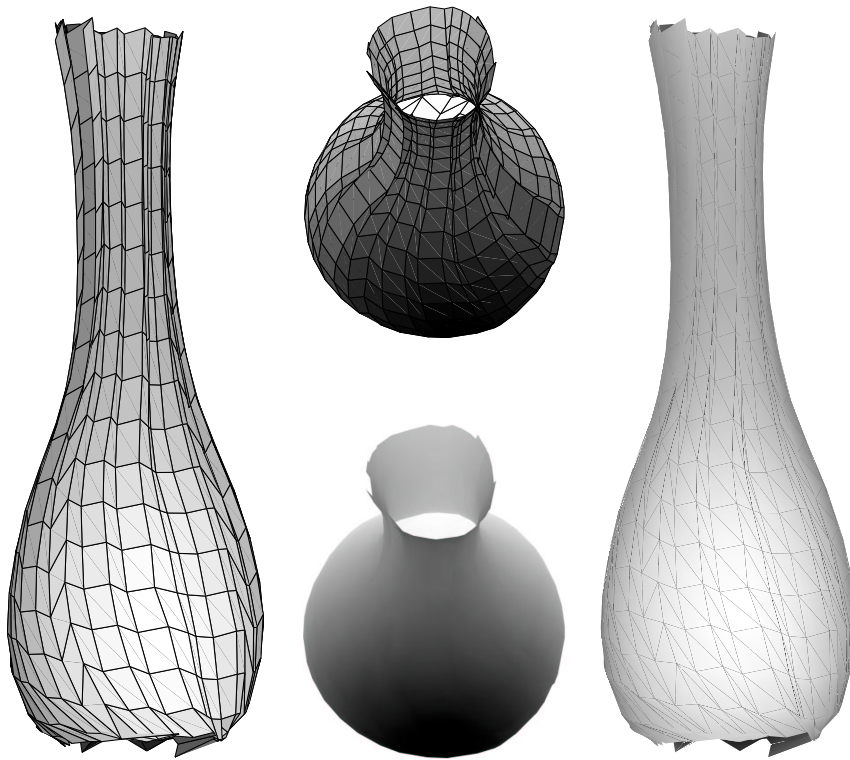


Figure 14: Details of the reconstruction of the vase by triangulating the profiles, using the method described in [39]. The model was built using 1224 triangles.

reconstruction, no point tracking is required and it does not depend on having point correspondences beforehand.

The convergence to local minima, a critical issue in most non-linear optimization problems, is avoided by a divide-and-conquer approach which keeps the size of the problem manageable. Moreover, a search space with lower dimension results in fewer iterations before convergence. The quality of model reconstructed is remarkable, in particular if one considers that only the least possible amount of information has been used. Since then the method has been applied to a large number of sequences, including human heads and sculptures.

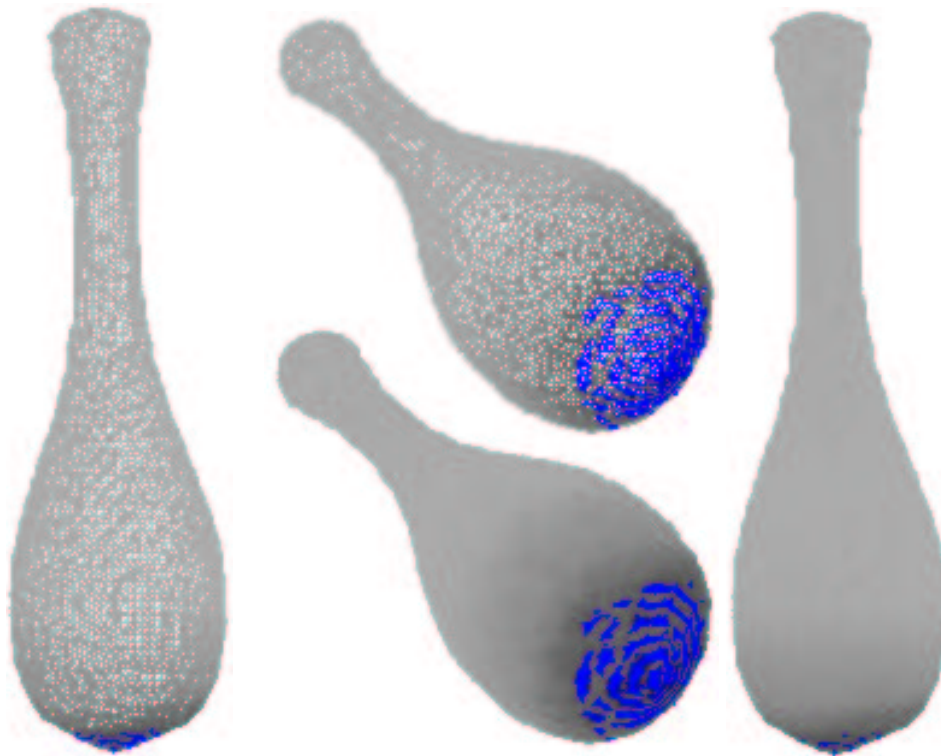


Figure 15: Details of the reconstruction of the vase by voxel carving, using the method described in [33], showing the triangular mesh and texture mapping. The model was built using 23144 triangles.

## 7.1 Future Work

An interesting problem is the development of an optimal solution for the problem of structure and motion from profiles — so far, there is no equivalent of a bundle adjustment algorithm capable of dealing with profiles. An important step in filling this gap is to develop a model for the effect that image noise has on the detection of profiles, and only when such error model becomes available a *maximum likelihood estimator* for structure and motion from profiles can be developed.

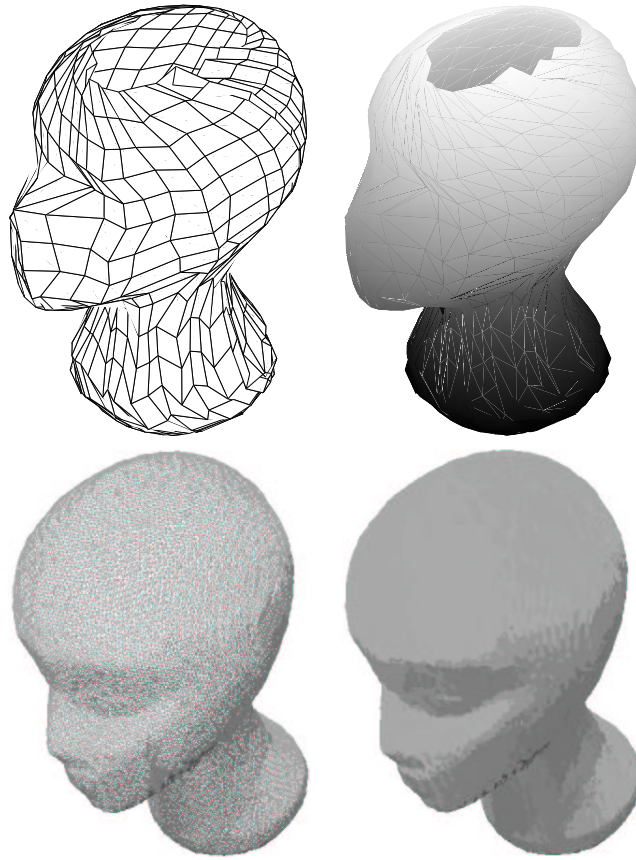


Figure 16: Details of the reconstruction of the head. The top row shows the reconstruction from the triangulation of the profiles, and the bottom row shows the result of voxel-carving. There are 1224 and 73736 triangles in the triangulated and the carved models, respectively.

## 8 Acknowledgements

Paulo R. S. Mendonça would like to acknowledge the financial support of CAPES, Brazilian Ministry of Education, grant BEX1165/96-8.

## References

- [1] K. Åström, R. Cipolla, and P. Giblin. Generalised epipolar constraints. *Int. Journal of Computer Vision*, 33(1):51–72, September 1999.

- [2] K. Åström, R. Cipolla, and P. J. Giblin. Generalised epipolar constraints. In B. F. Buxton and R. Cipolla, editors, *Proc. 4th European Conf. on Computer Vision*, volume II of *Lecture Notes in Computer Science 1065*, pages 97–108, Cambridge, UK, April 1996. Springer-Verlag.
- [3] E. Boyer and M. O. Berger. 3D surface reconstruction using occluding contours. *Int. Journal of Computer Vision*, 22(3):219–233, March/April 1997.
- [4] J. F. Canny. A computational approach to edge detection. *IEEE Trans. Pattern Analysis and Machine Intell.*, 8(6):679–698, November 1986.
- [5] T. J. Cham and R. Cipolla. Geometric saliency of curve correspondences and grouping of symmetric contours. In B. F. Buxton and R. Cipolla, editors, *Proc. 4th European Conf. on Computer Vision*, volume I of *Lecture Notes in Computer Science 1064*, pages 385–398, Cambridge, UK, April 1996. Springer-Verlag.
- [6] R. Cipolla, K. Åström, and P. J. Giblin. Motion from the frontier of curved surfaces. In *Proc. 5th Int. Conf. on Computer Vision*, pages 269–275, Cambridge, USA, June 1995.
- [7] R. Cipolla and A. Blake. Surface shape from the deformation of apparent contours. *Int. Journal of Computer Vision*, 9(2):83–112, November 1992.
- [8] R. Cipolla and P. J. Giblin. *Visual Motion of Curves and Surfaces*. Cambridge University Press, Cambridge, UK, 1999.
- [9] R. Cipolla, Y. Okamoto, and Y. Kuno. Robust structure from motion using motion parallax. In *Proc. 4th Int. Conf. on Computer Vision*, pages 374–382, Berlin, Germany, May 1993.
- [10] H. S. M. Coxeter. *Introduction to Geometry*. John Wiley and Sons, New York, 2<sup>nd</sup> edition, 1969.
- [11] G. Cross, A. Fitzgibbon, and A. Zisserman. Parallax geometry of smooth surfaces in multiple views. In *Proc. 7th Int. Conf. on Computer Vision*, volume I, pages 323–329, Corfu, Greece, September 1999.
- [12] R. W. Curwen, C. V. Stewart, and J. L. Mundy. Recognition of plane projective symmetry. In *Proc. 6th Int. Conf. on Computer Vision*, pages 1115–1122, Bombay, India, January 1996.
- [13] O. D. Faugeras. *Three-Dimensional Computer Vision: a Geometric Viewpoint*. Artificial Intelligence Series. MIT Press, Cambridge, USA, 1993.



- [14] A. W. Fitzgibbon, G. Cross, and A. Zisserman. Automatic 3D model construction for turn-table sequences. In R. Koch and L. Van Gool, editors, *3D Structure from Multiple Images of Large-Scale Environments, European Workshop SMILE'98*, Lecture Notes in Computer Science 1506, pages 155–170, Freiburg, Germany, June 1998. Springer-Verlag.
- [15] P. J. Giblin, F. E. Pollick, and J. E. Rycroft. Recovery of an unknown axis of rotation from the profiles of a rotating surface. *J. Opt. Soc. America A*, 11(7):1976–1984, July 1994.
- [16] P. J. Giblin and R. S. Weiss. Reconstruction of surfaces from profiles. In *Proc. 1st Int. Conf. on Computer Vision*, pages 136–144, London, June 1987.
- [17] P. J. Giblin and R. S. Weiss. Epipolar fields on surfaces. In J.-O. Eklundh, editor, *Proc. 3rd European Conf. on Computer Vision*, volume I of *Lecture Notes in Computer Science 800*, pages 14–23, Stockholm, Sweden, May 1994. Springer-Verlag.
- [18] R. Hartley. Projective reconstruction and invariants from multiple images. *IEEE Trans. Pattern Analysis and Machine Intell.*, 16(10):1036–1041, October 1994.
- [19] T. Joshi, N. Ahuja, and J. Ponce. Structure and motion estimation from dynamic silhouettes under perspective projection. *Int. Journal of Computer Vision*, 31(1):31–50, February 1999.
- [20] T. Kanade and J. R. Kender. Mapping image properties into shape constraints: Skewed symmetry, affine-transformable patterns, and the shape-from-texture paradigm. In J. Beck, B. Hope, and A. Rosenfeld, editors, *Human and Machine Vision*, pages 237–257. Academic Press, New York, 1983.
- [21] R. Koch, M. Pollefeys, and L. Van Gool. Multi viewpoint stereo from uncalibrated video sequences. In H. Burkhardt and B. Neumann, editors, *Proc. 5th European Conf. on Computer Vision*, volume I of *Lecture Notes in Computer Science 1406*, pages 55–71, Freiburg, Germany, June 1998. Springer-Verlag.
- [22] J. J. Koenderink. What does the occluding contour tell us about solid shape? *Perception*, 13:321–330, 1984.
- [23] K. N. Kutulakos and S. M. Seitz. A theory of shape by space carving. In *Proc. 7th Int. Conf. on Computer Vision*, volume I, pages 307–314, Corfu, Greece, September 1999.

- [24] J. Liu, J. Mundy, D. Forsyth, A. Zisserman, and C. Rothwell. Efficient recognition of rotationally symmetric surfaces and straight homogeneous generalized cylinders. In *Proc. Conf. Computer Vision and Pattern Recognition*, pages 123–129, New York, June 1993.
- [25] Q.-T. Luong and O. D. Faugeras. The fundamental matrix: Theory, algorithms, and stability analysis. *Int. Journal of Computer Vision*, 17(1):43–75, January 1996.
- [26] P. R. S. Mendonça, K.-Y. K. Wong, and R. Cipolla. Camera pose estimation and reconstruction from image profiles under circular motion. In David Vernon, editor, *Proc. 6th European Conf. on Computer Vision*, volume II of *Lecture Notes in Computer Science 1842*, pages 864–877, Dublin, Ireland, June/July 2000. Springer–Verlag.
- [27] D. P. Mukherjee, A. Zisserman, and J. M. Brady. Shape from symmetry—detecting and exploiting symmetry in affine images. In *Phil. Trans. Royal Soc. London A*, volume 351, pages 77–106, 1995.
- [28] V. S. Nalwa. Line-drawing interpretation: Bilateral symmetry. *IEEE Trans. Pattern Analysis and Machine Intell.*, 11(10):1117–1120, October 1989.
- [29] J. Porrill and S. B. Pollard. Curve matching and stereo calibration. *Image and Vision Computing*, 9(1):45–50, February 1991.
- [30] J. H. Rieger. Three dimensional motion from fixed points of a deforming profile curve. *Optics Letters*, 11(3):123–125, March 1986.
- [31] J. Sato and R. Cipolla. Affine reconstruction of curved surfaces from uncalibrated views of apparent contours. *IEEE Trans. Pattern Analysis and Machine Intell.*, 21(11):1188–1198, November 1999.
- [32] J. G. Semple and G. T. Kneebone. *Algebraic Projective Geometry*. Oxford Classic Texts in the Physical Sciences. Clarendon Press, Oxford, UK, 1998. Originally published in 1952.
- [33] R. Szeliski. Rapid octree construction from image sequences. *Computer Vision, Graphics and Image Processing*, 58(1):23–32, July 1993.
- [34] R. Szeliski and R. Weiss. Robust shape recovery from occluding contours using a linear smoother. *Int. Journal of Computer Vision*, 28(1):27–44, June 1998.
- [35] C. Tomasi and T. Kanade. Shape and motion from image streams under orthography: A factorization method. *Int. Journal of Computer Vision*, 9(2):137–154, November 1992.

- [36] B. Triggs. Plane + parallax, tensors and factorization. In D. Vernon, editor, *Proc. 6th European Conf. on Computer Vision*, volume I of *Lecture Notes in Computer Science 1842*, pages 522–538, Dublin, Ireland, June/July 2000. Springer-Verlag.
- [37] R. Vaillant and O. D. Faugeras. Using extremal boundaries for 3D object modelling. *IEEE Trans. Pattern Analysis and Machine Intell.*, 14(2):157–173, February 1992.
- [38] T. Vieville and D. Lingrand. Using specific displacements to analyze motion without calibration. *Int. Journal of Computer Vision*, 31(1):5–29, February 1999.
- [39] K.-Y. K. Wong, P. R. S. Mendonça, and R. Cipolla. Reconstruction and motion estimation from apparent contours under circular motion. In T. Pridmore and D. Elliman, editors, *Proc. British Machine Vision Conference*, volume 1, pages 83–92, Nottingham, UK, September 1999.
- [40] Z. Zhang. Determining the epipolar geometry and its uncertainty: A review. *Int. Journal of Computer Vision*, 27(2):161–195, March/April 1998.
- [41] A. Zisserman, D. Forsyth, J. L. Mundy, and C. A. Rothwell. Recognizing general curved objects efficiently. In J. L. Mundy and A. Zisserman, editors, *Geometric Invariance in Computer Vision*, Artificial Intelligence Series, chapter 11, pages 228–251. MIT Press, Cambridge, USA, 1992.